Electrochemical Activation and Functionalization of the Uranyl Ion

Riddhi R. Golwankar,[a] Małgorzata Z. Makoś,[b] Nathalia Cajiao,[c] Michael L. Neidig,[c,d] Allen G. Oliver,[e] Cynthia S. Day,[f] Victor W. Day,[a] Vassiliki-Alexandra Glezakou,[b,*] and James D. Blakemore[a,*]

[a] Department of Chemistry, University of Kansas, 1567 Irving Hill Road, Lawrence, Kansas 66045, United States

[b] Chemical Sciences Division, Oak Ridge National Laboratory, Oak Ridge, Tennessee 37830, United States

[c] Department of Chemistry, University of Rochester, 120 Trustee Road, Rochester, New York 14627, United States

[d] Inorganic Chemistry Laboratory, Department of Chemistry, University of Oxford, South Parks Road, Oxford, United Kingdom

[e] Department of Chemistry and Biochemistry, University of Notre Dame, Notre Dame, Indiana 46556, United States

[f] Department of Chemistry, Wake Forest University, Winston–Salem, North Carolina 27109, United States

ABSTRACT: Interconversion of the oxidation states of uranium enables separations and reactivity schemes involving this element and contributes to technologies for recycling of spent nuclear fuels. The redox behaviors of uranium species impact these processes, but use of electrochemical methods to drive reactions of well-defined precursors and to obtain molecular insights into the outcomes has received less attention than it deserves. Here, we show that electro-reduction of the uranyl ion (UO_2^{2+}) can be used to promote stepwise functionalization of the typically unreactive oxo groups with exogenous triphenylborane (BPh_3) serving as a moderate electrophile. Parallel electroanalytical, spectrochemical, and chemical reactivity studies, supported by spectroscopic findings and structural data from X-ray diffraction analysis on key reduced and borylated products, demonstrate that our electrochemical approach largely avoids undesired cross reactions and disproportionation pathways; these conventionally impact the multicomponent systems needed for uranyl functionalization chemistry. Joint computational studies have been used to map the mechanistic pathways involved in this U–O activation, and to quantify free energy changes associated with key reactions. Taken together, the results suggest that electrochemical methods can be used for selective interconversion of molecular actinide species, reminiscent of methods commonly employed in transition metal redox catalysis.

Development of electrochemically driven routes for desirable transformations that could replace older chemical technologies is attracting significant attention in a variety of fields, including electrosynthesis of organic compounds and carbon capture/utilization.[1] In these cases, electrochemical methods can enable replacement of stoichiometric reagents with "greener" analogues, allow improved product yield through avoidance of forcing conditions, and favor selectivity through use of modest overpotentials. These advantages are making electrochemical methods attractive for exploration across the chemical enterprise, particularly for challenging reactions that are difficult to achieve by conventional chemical means.

One such challenging reaction is reductive activation of high-valent uranium and processing of this element into stable lower-valent forms. The uranyl ion (UO_2^{2+}) is a unique species from this perspective, as although it features high-valent uranium that has lost all its valence electrons, the uranyl ion is a very weak oxidant that is resistant to reduction ($E°(U^{VI/V})$ = 0.16 V vs. NHE in acid).[2] The uranyl ion is highly water soluble, however, impacting remediation and storage of nuclear materials.[3,4] Moreover, the U–O bond dissociation energy has been estimated at *ca.* 133 kcal mol^{-1}, in line with observations spanning decades that this dication is thermodynamically stable and typically inert to chemical reactions.[5] Consequently, these oxo groups are challenging to either functionalize[6,7] or more simply to protonate; UO_2^{2+} does not undergo protonation at the oxo moieties even in neat triflic acid (pK_a = 0.7 in MeCN).[8]

Appealingly, however, chemical studies have shown that reduction of U(VI) to U(V) can facilitate oxo functionalization (Scheme 1). Mazzanti and co-workers first demonstrated chemical isolation and study of uranium(V) complexes early in the 21st century,[9] laying the groundwork for exploration of reactivity in this realm through their finding that the oxo ligands become more basic upon reduction of uranium.[10] A landmark report from Arnold, Love, and co-workers[11] showed that simultaneous treatment of a macrocyclic UO_2^{2+} complex with KH (a strong reducing agent) and trimethylsilylamide (an electrophile that forms a strong Si–O bond) results in selective silylation of a uranium-oxo moiety coupled to reduction of U(VI) to U(V). In this system, reduction by KH to generate U(V) occurred only upon formation of the Si–O bond. In several key reports, Hayton and co-workers demonstrated the use of the strong electrophile tris(pentafluorophenyl)borane, i.e. $B(C_6F_5)_3$, for oxo functionalization of the uranyl ion[12,13]; Hayton's group has also utilized R_3SiH (R = Ph or Et) as a combined reductant and silylating reagent for oxo functionalization.[14,15] Taken together, these reports highlight the usefulness of chemical reduction and electrophile-coupled chemistry in achieving U–O bond functionalization.[16]

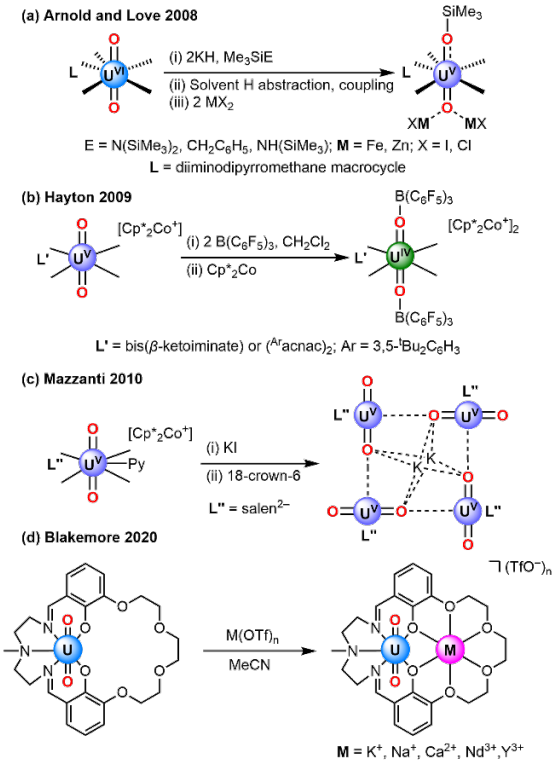

Scheme 1. Selected literature examples of chemistries for activation and functionalization of the uranyl ion.

However, a unifying theme of literature work on uranyl functionalization is the apparent requirement of strong chemical reductants as well as highly electrophilic co-reactants to achieve U–O activation. This is consistent with the rather negative standard reduction potential of the uranyl ion, but as use of very strong reductants drives energetic losses and unselective reaction channels, such chemical approaches to this reactivity remain suboptimal. In prior work, modulation of the reduction potential of the uranyl ion in heterobimetallic complexes was studied by Blakemore and co-workers,[17] as a window to accessing new reactivity. Solvent-driven cross-reactivity that can occur in uranyl reduction chemistry has also been studied.[18]

Considering these observations regarding chemical redox work with the uranyl ion, our attention was drawn to the possibility of study of electrochemical conditions for uranyl activation and functionalization. In considering the setup of such conditions, we imagined that energetic losses could be minimized through application of minimal overpotentials, particularly if electron transfer to the uranyl species targeted for activation were facile. We also imagined that clean generation of U(V) could be used to trigger oxo functionalization, thus avoiding a need for electrophile pre-coordination as well as disfavoring direct electrophile reduction/decomposition. Studies of electrode-induced reactivity of the uranyl ion would also build on existing studies of uranyl redox chemistry tuned by coordination changes,[19] as well as ongoing work examining use of molten salt electrolysis for actinide processing.[20]

Here, we report an electrochemical scheme for activation and functionalization of the uranyl ion, UO_2^{2+}, in the polar, organic solvent acetonitrile. In this scheme, electro-reduction of a U(VI) precursor by 1e$^-$ results in generation of a species in the U(V) formal oxidation state that can undergo reaction with triphenylborane (BPh_3). On the basis of electrochemical titration data, the uranyl ion can be readily functionalized at the electrode surface to form either mono- or bis-borylated species. Comprehensive electrochemical, spectrochemical and spectro-electrochemical studies have been used to reveal the highly selective nature of the stepwise reaction sequence involved in accessing these borylated complexes, a sequence which begins in all cases with reduction, as BPh_3 does not react with the parent UO_2^{2+} complex or undergo direct electro-reduction at relevant potentials in MeCN-based electrolyte. Exploration of the chemistry of this system from the standpoint of both experimental and computational studies suggests that electrochemical methods offer a useful route for selective interconversion of uranium species and opportunities for mechanistic insight that are challenging to access in purely chemical work.

Results

Redox Chemistry of Uranyl Reduction

At the outset of our investigation, we sought to prepare a U(VI) starting material appropriate for studies of oxo functionalization (Scheme 2). The core uranyl-binding motif that we previously utilized in a macrocyclic ligand[17] seemed appropriate for this purpose; this core, denoted ^{Me}saldien, has been used previously in the literature for complexation of UO_2^{2+} in pyridine[21] and ethanol[22] but not isolated. However, as this ligand can be pentadentate and favors solvent exposure of the oxo moieties, it was ideal for our purpose. Thus, we developed procedures for isolation of ^{Me}saldien (Figures S1 and S2) and a procedure for generation of its corresponding U(VI) complex, denoted **U^{VI}** (Figures S3 and S4). Our procedure for preparation of **U^{VI}** utilizes $UO_2(OAc)_2{\bullet}2H_2O$ as the metal-containing precursor in light of its reliable protonolysis behavior.[17,23] ^{1}H NMR data reveal that **U^{VI}** displays C_{2v} symmetry in d_3-MeCN, consistent with κ^5 coordination of ^{Me}saldien; the ^{1}H NMR spectrum features a singlet at 3.22 ppm (integrating to 3H) that corresponds to the methyl protons of the tertiary amine (Figure S3). Installation of this methyl group avoids the presence of a potentially ionizable proton in the ligand backbone, as in a more well-known analogue of this ligand.[24] These data are also consistent with a prior X-ray diffraction (XRD) structure of **U^{VI}** (grown from pyridine/hexane solution)[21] showing κ^5 coordination of ^{Me}saldien in the equatorial plane of UO_2^{2+}.

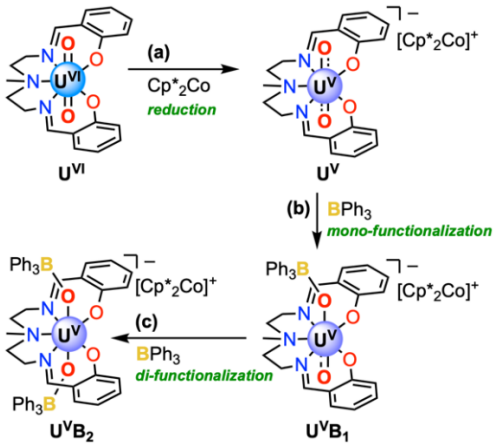

Scheme 2. Interconversions of forms of the uranyl ion studied in this work: (a) Reduction to generate U^V from U^{VI}; (b) mono-functionalization with BPh_3 to generate U^{V}B$_1$; (c) di-functionalization with BPh_3 to generate U^{V}B$_2$.

Cyclic voltammetry (CV) data collected for **U^{VI}** reveal a single quasi-reversible reduction feature with $E_{1/2}$ = −1.55 V vs.

ferrocenium/ferrocene (denoted hereafter as $Fc^{+/0}$) in MeCN solution containing 0.1 M tetrabutylammonium hexafluorophosphate as the supporting electrolyte (Figure 1, panel a and Figure S24). Consistent with the soluble nature of $\mathbf{U^{VI}}$, the peak currents for both the cathodic and anodic processes associated with this wave were found to be linearly dependent on the square-root of scan rate (Figure S25). The peak-to-peak separation of the anodic and cathodic processes (ΔE_p) was 79 mV at 100 mV/s scan rate, consistent an electrochemically quasi-reversible process in which the oxidized and reduced forms of $\mathbf{U^{VI}}$ undergo rapid interconversion at the electrode surface.[25,26] As the ratio of the anodic to cathodic peak currents is near unity for all scan rates that we tested (Figure S26), we conclude that the reduction of $\mathbf{U^{VI}}$ is chemically reversible. On the basis of prior studies of related complexes from our group and others,[28] the reduction of $\mathbf{U^{VI}}$ can be anticipated to be $1e^-$ in nature, resulting in generation of a complex, denoted $\mathbf{U^{V}}$, that features uranium in the +V formal oxidation state (for further characterization, *vide infra*).

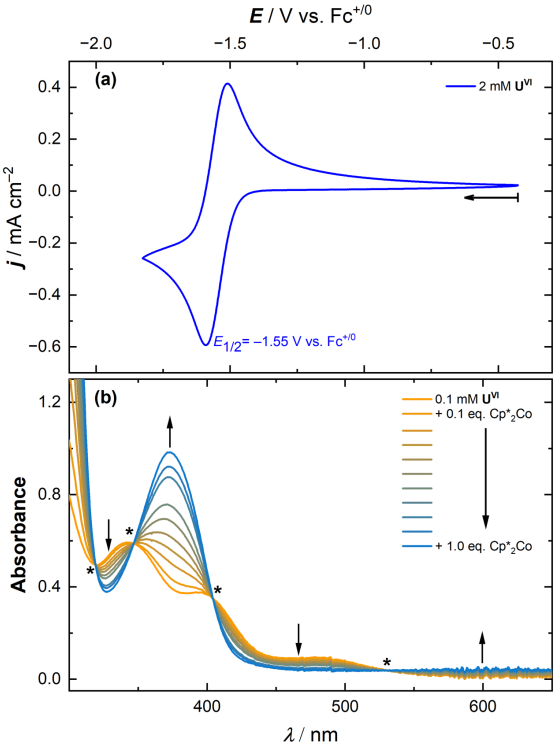

Figure 1. Panel a: Cyclic voltammetry data for $\mathbf{U^{VI}}$ in MeCN (0.1 M $[^nBu_4N]^+[PF_6]^-$, 100 mV/s). Panel b: Spectrochemical titration data for $\mathbf{U^{VI}}$ with 1 equiv. of Cp^*_2Co in MeCN. Isosbestic points are indicated with asterisk (*) and located at 319, 347, 404, and 531 nm.

To confirm the $1e^-$ nature of the reduction process measured for $\mathbf{U^{VI}}$, we carried out a spectrochemical titration with UV-visible (UV-vis) monitoring using the strong outer-sphere chemical reductant decamethylcobaltocene (Cp^*_2Co). We chose Cp^*_2Co on the basis of its rather negative reduction potential,[27] measured under our conditions to be $E_{1/2}$ ($Cp^*_2Co^{+/0}$) = −1.91 V vs $Fc^{+/0}$ (Figures S27 and S28). Considering the more positive reduction potential measured for reduction of $\mathbf{U^{VI}}$ to $\mathbf{U^{V}}$, addition of Cp^*_2Co to $\mathbf{U^{VI}}$ should result in electron transfer; the driving force for $\mathbf{U^{V}}$ generation can be estimated at –8.3 kcal mol^{-1}. The UV-vis spectrum of isolated $\mathbf{U^{VI}}$ at 100 μM displays two prominent absorption features with $\lambda_{max} \approx 344$ and 399 nm (Figure S42), but upon addition of Cp^*_2Co up to 1 equivalent per $\mathbf{U^{VI}}$, significant changes occurred in the spectrum (Figure 1, panel b). The most obvious change is the isosbestic growth of a new transition with λ_{max} = 373 nm, corresponding to generation of $\mathbf{U^{V}}$. The feature at 373 nm is similar to those measured for structurally related, formally U(V) uranyl complexes in literature.[28,29] Clean one-electron reduction of $\mathbf{U^{VI}}$ is evident from the isosbestic points at 278, 319, 347, 404, and 531 nm (Figure 1, panel b, and Figure S45), as well as from the observation that further additions of Cp^*_2Co beyond 1 equiv. did not drive further changes in the absorption features corresponding to the uranium species in solution (Figure S47). These data for further additions showed only the persistence of Cp^*_2Co in solution, consistent with the lack of reduction beyond $\mathbf{U^{V}}$ in the CV studies.

Clean generation of $\mathbf{U^{V}}$ by $1e^-$ reduction of $\mathbf{U^{VI}}$ could also be confirmed under electrochemical conditions through spectroelectrochemical experiments. Spectral changes resembling those observed in the chemical titration described above were observed (corresponding to $\mathbf{U^{VI}}$ reduction at the electrode) upon polarization of a platinum flag electrode in a thin-layer cuvette cell at –1.7 V (see Experimental Section and Figure S68 for details). The noted potential is sufficiently negative to drive conversion of $\mathbf{U^{VI}}$ to $\mathbf{U^{V}}$, evident in the UV-vis data from isosbestic points found at 351, 402, and 547 nm (Figure S69); these values are similar to some of those measured in the case of the titration with Cp^*_2Co, in line with the similar absorption profiles that would be expected for the products generated in each case. The product of electrochemical reduction would be $[U^V]^-NBu_4^+$ whereas in chemical work it is $[U^V]^-Cp^*_2Co^+$. In the electrochemical case, we note here that an overpotential of only 150 mV was used to generate the reduced form at the electrode.

Electrochemical Studies of Uranyl Functionalization

With the above data in hand showing that $\mathbf{U^{V}}$ is generated cleanly under both chemical and electrochemical conditions, we turned our attention to electroanalytical interrogation of the reactivity of $\mathbf{U^{V}}$ with our selected electrophile, triphenyl borane (BPh_3). As mentioned in the Introduction, prior reports have shown that adding a Lewis acidic reaction partner to uranyl species can enable weakening of the U–O interaction.[11,12,21] We were initially inspired to work with BPh_3 as it is less Lewis acidic (by ca. 7 orders of magnitude[30]) than the more commonly investigated electrophile $B(C_6F_5)_3$. BPh_3 retains the appealing bulky, triaryl nature of $B(C_6F_5)_3$, however, enabling studies with controlled acid-base stoichiometry.

To probe for electrochemically induced oxo activation and functionalization, we performed a titration with BPh_3 using CV (Figure 2). As described above, the CV profile for a solution containing 2 mM $\mathbf{U^{VI}}$ displays a single, chemically reversible wave corresponding to generation of $\mathbf{U^{V}}$ at the electrode surface. However, upon addition of BPh_3 to the electrochemical cell in increments of 0.2 equiv. per $\mathbf{U^{VI}}$ and interrogation of the accessible redox chemistry by CV, we observed that the current corresponding to re-oxidation of $\mathbf{U^{V}}$ ($E_{p,a}$ = –1.51 V; see Figure 2, panel a) decreases as the amount of BPh_3 present in the cell increases. This implies that $\mathbf{U^{V}}$, the immediate product of reduction of $\mathbf{U^{VI}}$, is consumed by a chemical reaction involving BPh_3 before it can undergo re-oxidation on the return anodic sweep. In other words, $\mathbf{U^{V}}$ is depleted from the reaction-diffusion layer at the electrode surface by the chemical reaction with borane; this profile is consistent with so-called *EC-type* behavior,[26] meaning that a fast electrochemical reduction (*E*) is followed by a follow-up chemical reaction (*C*). We observed that the return oxidation wave was diminished completely upon addition of 1 to 1.2 equiv. of BPh_3,

suggestive of adduct formation upon generation of $\mathbf{U^V}$ that results in new species with shifted redox properties.

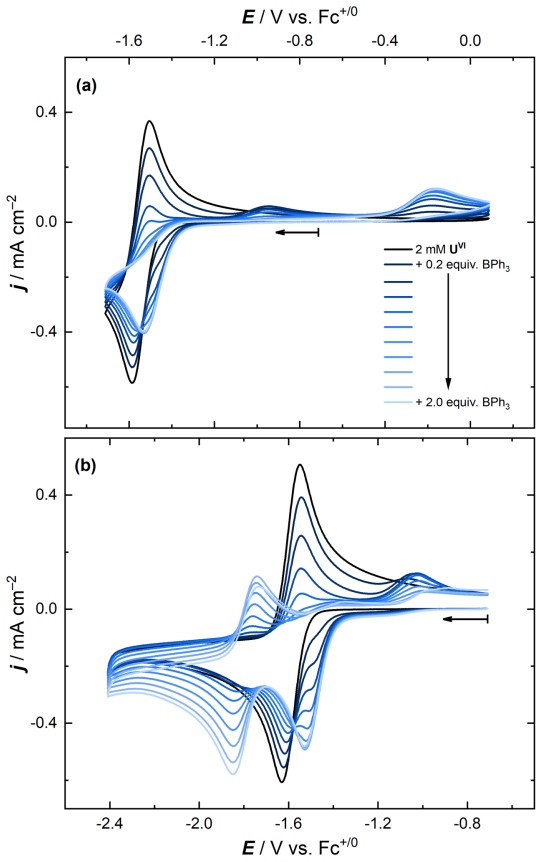

Figure 2. Cyclic voltammetry titration data for 2 mM solution of $\mathbf{U^{VI}}$ with BPh_3 in MeCN (0.1 M $[^nBu_4N]^+[PF_6]^-$, 100 mV/s).

However, in addition to this change in anodic current, we also observed that the reduction wave associated with $\mathbf{U^V}$ generation (with initial $E_{p,c}$ = –1.59 V) undergoes an obvious shift to a more positive potential as the concentration of BPh_3 increases. The data for the cathodic wave display a pivot point (or isogalvanic potential) at ca. E = –1.58 V and j = –0.41 mA cm^{-2}. This profile is consistent with contribution of a kinetic potential shift to the U(VI)/U(V) reduction wave. Such shifts arise from rapid depletion of nascent $\mathbf{U^V}$ from the reaction-diffusion layer near the electrode surface; perturbation of the Nernst equilibrium for the $\mathbf{U^{VI}/U^V}$ manifold is occurring as a result of the *EC-type* behavior, leading to a positive shift in the measured cathodic potential.[26] Comparison with literature examples confirms the profile of our data, including the isogalvanic potential, are consistent with *EC-type* behavior.[31] This behavior, wherein $\mathbf{U^V}$ reacts with BPh_3, contrasts with prior work showing reaction of U(VI) complexes with $B(C_6F_5)_3$.[13,32] Importantly, results from both UV-visible and ^{1}H NMR spectroscopies confirm that BPh_3 does not react with $\mathbf{U^{VI}}$ in either MeCN or our electrolyte (Figures S10-S11 and S49-S51). This is consistent with the lower Lewis basicity of the terminal oxo ligands in the U(VI) oxidation state vs. U(V), as well as coordination of MeCN to BPh_3 under our experimental conditions, as suggested by results from infrared spectroscopy (Figures S58 and S59).

At the outset of this investigation, we hypothesized that borylation could occur in our complex at one or both of the uranyl oxo ligands, owing to the anticipated lack of steric bulk above and below the plane of the ^{Me}saldien ligand (Scheme 2). In accord with this hypothesis, two new anodic waves appear in the voltammetry data collected in the presence of BPh_3. The first of these is apparent at $E_{p,a}$ = –0.95 V, while the second occurs at a more positive potential with $E_{p,a}$ = –0.16 V (Figure 2, panel a, Figure S33, and S35). Both these waves are located at peak potentials which are more positive than the initial $\mathbf{U^{VI}/U^V}$ redox wave, implying that the species undergoing oxidation feature weaker sets of donating ligands than in the starting complex. Control experiments in which the cathodic switching potential was set *positive* of that required to affect generation of $\mathbf{U^V}$ confirmed that generation of this species is required to observe the new anodic waves (Figure S37).

These observations are consistent with sequential *in situ* borylation of the oxo ligands of electrogenerated $\mathbf{U^V}$; the shifts in the measured anodic potentials (ΔE) of +0.56 V and +1.35 V correspond to observation of the U(V) to U(VI) waves for mono- and bis-borylated species derived from reaction of $\mathbf{U^V}$ with BPh_3. The shift in potential upon bis-borylation is approximately double that encountered for mono-borylation ($\Delta E_{bis}/\Delta E_{mono}$ = 2.4), in accord with the proposed reaction stoichiometry. Also, in accord with our proposal, Arnold, Love, and co-workers have recently measured a +0.69 V shift in $E(U^{VI}/U^V)$ between synthetically isolated non-borylated and mono-borylated complexes bearing a diypyrromethene-based ligand.[19]

Examining the $[BPh_3]$ dependence of the CV titration data, the current density associated with the more negative of the two new anodic features is maximized at moderate BPh_3 concentrations (ca. 0.4 equiv.) while the more positive wave is maximized at 2.0 equiv. Furthermore, addition of BPh_3 beyond 2.0 equiv. does not result in significant changes in the voltammetry. With all this in mind, the feature with $E_{p,a}$ = –0.95 V could be assigned as oxidation of a mono-borylated species derived from $\mathbf{U^V}$ (denoted $\mathbf{U^VB_1}$; see Scheme 2) and the feature with $E_{p,a}$ = –0.16 V as oxidation of a bis-borylated species (denoted $\mathbf{U^VB_2}$). Qualitatively, the appearance of the incipient anodic waves for $\mathbf{U^VB_1}$ and $\mathbf{U^VB_2}$ is consistent with rapid electron transfer for these species, similar to the behavior encountered with isolated $\mathbf{U^{VI}}$.

Examination of multi-cycle CV data measured with $\mathbf{U^{VI}}$ in the presence of added BPh_3 enables investigation of the chemical reversibility of the apparent U(VI)/U(V) redox manifolds for $\mathbf{U^VB_1}$ and $\mathbf{U^VB_2}$. At 100 mV/s, the oxidations of both $\mathbf{U^VB_1}$ and $\mathbf{U^VB_2}$ appear irreversible, in that a wave corresponding to reduction of the U(VI) forms of these species is absent in the 2nd and subsequent cycles of voltammetry (Figures S38 and S39). As the appearance of the reduction wave of $\mathbf{U^{VI}}$ is unchanged upon carrying out multiple cycles of voltammetry, the products of oxidation of $\mathbf{U^VB_1}$ and $\mathbf{U^VB_2}$ appear to quickly lose the associated equivalent(s) of BPh_3 upon oxidation. This proposal is consistent with computational results showing that generation of U(VI) in these systems results in B–O_{oxo} bond cleavage rather than U–O_{oxo} cleavage (*vide infra*). All of these observations amount to evidence of a well-defined series of redox-induced processes displayed by our complexes; these are shown in Scheme 3.

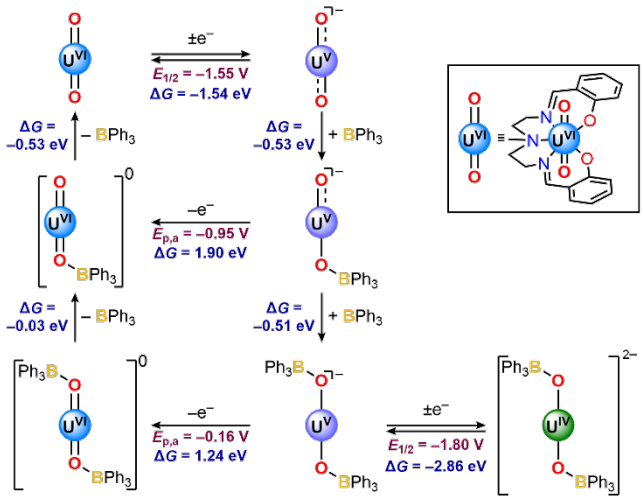

Scheme 3. Redox-promoted uranyl reactivity pathways described in this work. Measured potentials from CV data are given in purple text and are reported vs. ferrocenium/ferrocene. Calculated Gibbs free energies, ΔG, from theoretical calculations with Cp^*_2Co as chemical reductant are given in royal blue text.

Extension of these electrochemical studies to much faster scan rates was also pursued in attempt to observe re-reduction of the U(VI) species derived from $\mathbf{U^VB_1}$ and $\mathbf{U^VB_2}$. At scan rates above 500 mV/s, return waves could be measured that pair well with the oxidation peaks measured for both $\mathbf{U^VB_1}$ and $\mathbf{U^VB_2}$ (Figures S40 and S41). Thus, the loss of BPh_3 appears slow enough that re-reduction of these species can be directly interrogated. Moreover, the $E_{1/2}$ values for U(VI)/U(V) cycling of both $\mathbf{U^VB_1}$ and $\mathbf{U^VB_2}$ could be measured from this data, returning values of –0.91 V and –0.13 V, respectively, at 1000 mV/s (Table S2). The ΔE_p values measured for these waves are similar, around 20 mV, suggest that the electrogenerated species may display transient interactions with the electrode surface, despite the apparent solubility of chemically prepared $\mathbf{U^VB_1}$ and $\mathbf{U^VB_2}$ (*vide infra*).

In addition to these changes, a new wave also appears at more negative potentials in voltammograms collected with concentrations of BPh_3 beyond 0.8 equiv. This new quasi-reversible couple lies at $E_{1/2}$ = –1.80 V (Figure 2, panel b and S35) and displays a reasonable ΔE_p value at 100 mV/s of ca. 110 mV. Based upon the concentrations of BPh_3 at which this wave becomes obvious, and its measured potential, we hypothesize that double functionalization of $\mathbf{U^V}$ with BPh_3 enables the uranium center in $\mathbf{U^VB_2}$ to undergo further reduction, forming a species in the formal U(IV) oxidation state, denoted $\mathbf{U^{IV}B_2}$. For comparison, control experiments showed that BPh_3 itself undergoes an irreversible reduction at a potential of –2.38 V (Figure S32); this value is much more negative than that required to access $\mathbf{U^{IV}B_2}$ or any of the U(V) species discussed in this work. Consequently, use of our electrochemical approach and BPh_3 as a modest electrophile avoid undesirable cross-reactivity that could decrease the selectivity of the oxo-functionalization chemistry that we have observed.

Inspection of all the available CV data reveals that the $E_{1/2}(U^V/U^{IV})$ for $\mathbf{U^VB_2}$, –1.80 V, is significantly more negative than the estimated $E(U^{VI}/U^V)$ potential for this species, –0.13 V. This corresponds to a wide difference in potential of 1.67 V. To the best of our knowledge, thermodynamic potentials for U^{VI}/U^V and U^V/U^{IV} processes in a single uranyl-derived ligand framework with functionalized oxo ligands has not been previously measured. However, our values may compare well to measurements from Arnold, Love, and co-workers[19] for an unfunctionalized uranyl species that showed a gap between U^{VI}/U^V and U^V/U^{IV} of 840 mV; at this stage, we anticipate that the greater potential gap for our complex could be attributable to both the involvement of ligand-centered orbital involvement in the prior work (which could induce a redox-leveling effect and diminish the gap between oxidation states) as well as the anionic and dianionic nature of $\mathbf{U^VB_2}$ and $\mathbf{U^{IV}B_2}$, respectively, under investigation here. In any case, the wide potential gap between the U(VI) and U(IV) oxidation states in our system highlights the importance of ligand tuning as a strategy for oxo-functionalization and reductive processing of oxidic uranium species.

Optical Studies of Activation and Functionalization

In order to provide further evidence of the chemical reactivity pathways operating in our system, as observed in the electrochemical data, we carried out spectrochemical titration experiments. In these experiments, our goal was to directly measure changes in UV-visible spectra reporting on formation of the chemical species discussed above. In this approach, $\mathbf{U^V}$ was generated *in situ* by the reduction of isolated $\mathbf{U^{VI}}$ with 1 equiv. of Cp^*_2Co, which is sufficiently reducing to cleanly produce $\mathbf{U^V}$ (*vide supra*). Titration of $\mathbf{U^V}$ with increasing amounts of BPh_3 results in marked spectral changes up to one equivalent of borane, including diminished absorption in the transition centered at 372 nm (Figure 3, panel a). Isosbestic changes were measured at λ_{iso} = 321 nm, 422 nm, and 564 nm (Figure S52), consistent with clean generation of $\mathbf{U^VB_1}$ from $\mathbf{U^V}$. In accord with this conclusion, there is a uniform shift in the transition at 372 nm in the profile of $\mathbf{U^V}$ to 368 nm after the addition of 1 equiv. BPh_3 (Figure S54). Consequently, we conclude that under these conditions ([uranium] = 100 μM) $\mathbf{U^V}$ undergoes clean reactivity to produce $\mathbf{U^VB_1}$.

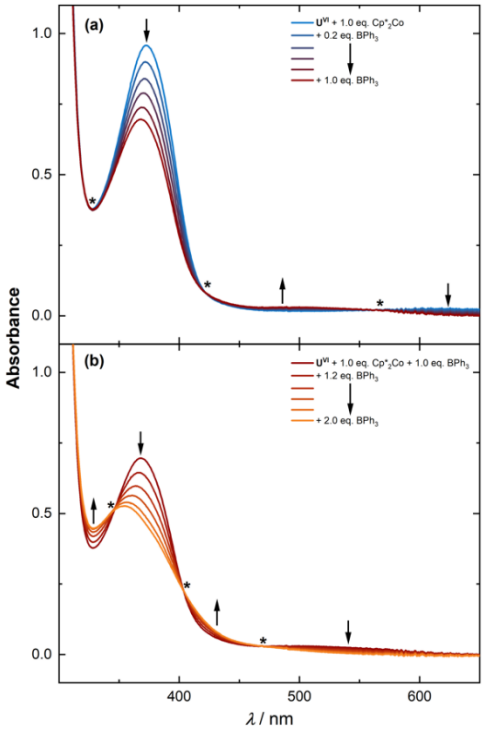

Figure 3. Panel a: Spectrochemical titration data for *in situ* generated $\mathbf{U^V}$ with 1 equiv. of BPh_3 in MeCN. Isosbestic points are indicated with

asterisk (*) and located at 321, 422, and 564 nm. Panel b: Spectrochemical titration data for further addition of BPh_3 up to 2 equiv. Isosbestic points are located at 347, 403, and 469 nm.

Further addition of BPh_3 in 0.2 equiv. increments suggests that $\mathbf{U^{V}B_1}$ reacts with a second BPh_3 to form $\mathbf{U^{V}B_2}$. UV-visible spectra for this transformation show a distinctive set of isosbestic points with λ_{iso} = 347, 403, and 469 nm (Figure 3, panel b and Figure S53). The noted strongly absorbing transition that was initially at 372 nm for $\mathbf{U^{V}}$ and shifted to 368 nm in the case of $\mathbf{U^{V}B_1}$ undergoes a further blue shift upon generation of $\mathbf{U^{V}B_2}$ to 354 nm (Figure S54). Similar to the case of $\mathbf{U^{V}B_1}$ these data support that $\mathbf{U^{V}B_2}$ can be cleanly generated when [uranium] = 100 μM as in this experiment.

These findings demonstrate that $\mathbf{U^{V}B_1}$ and $\mathbf{U^{V}B_2}$ can be produced cleanly at [U] = 100 μM, and that there is a clear dependence of the product obtained on the amount of borane added. The CV data (*vide supra*) are in agreement with this notion, in that the amount of borane added to the electrochemical cell influences the product distribution of the mono- and bis-borylated species. The mono- is accessible at low borane concentrations and the bis- is favored at higher concentrations. Computational results (*vide infra*) show that both the borylation reactions in our system are exergonic, in line with these experimental findings.

The spectrochemical data regarding formation of $\mathbf{U^{V}B_2}$ could be directly compared to an analogous spectroelectrochemical study examining generation of this species from $\mathbf{U^{VI}}$ and BPh_3. To detect the formation of $\mathbf{U^{V}B_2}$, two equivalents of borane were added to a solution of $\mathbf{U^{VI}}$ in electrolyte. Electrolysis of this solution at –1.65 V with simultaneous UV-visible monitoring revealed the growth of new absorption features with isosbestic behavior (Figures S71 and S72), confirming clean conversion of $\mathbf{U^{VI}}$ to $\mathbf{U^{V}B_2}$. The spectral profile of the spectroelectrochemically generated/observed $\mathbf{U^{V}B_2}$ agrees well with the spectrochemical data (Figure S74), particularly in the absorption feature centered near 3 nm. Consequently, we conclude that formation of the borylated species can be achieved under both chemical and electrochemical conditions and that complementary insights come from comparing the alternative reduction methods.

Chemical Synthesis and NMR Studies of the U(V) Complexes

Encouraged by the apparent stability of $\mathbf{U^{V}}$, $\mathbf{U^{V}B_1}$, and $\mathbf{U^{V}B_2}$ on the CV timescale, we attempted chemical preparation and isolation of these compounds in MeCN. To prepare $\mathbf{U^{V}}$, $\mathbf{U^{VI}}$ was treated with 1 equiv. of Cp^*_2Co in MeCN, resulting in a color change from orange to blue. The solvent was removed *in vacuo* yielding a greenish blue powder. The ^{1}H NMR spectrum (d_3-MeCN) of this material indicates formation of $[Cp^*_2Co]^+$ (singlet at δ ≈1.70 ppm), confirmed by comparison of the noted singlet to that found for commercially available $[Cp^*_2Co][PF_6]$ (Figures S6 and S8). Replicate measurements of 14 separate samples of $\mathbf{U^{V}}$ (including samples in which the compound was *in situ* generated or isolated as a powder and re-dissolved for analysis) over the course of this work gave the chemical shift for the $[Cp^*_2Co]^+$ counteraction associated with $\mathbf{U^{V}}$ a value of 1.719 ± 0.007 ppm, closely resembling the chemical shift of commercial $[Cp^*_2Co][PF_6]$ (δ = 1.699 ± 0.002 ppm across three replicate samples) (Table S1). These data indicate clean conversion of Co^{II} to Co^{III}, as the position of the peak corresponding to the Cp* methyl protons is sensitive to the oxidation state of Co (Figures S5-S7). Additionally, upon addition of Cp^*_2Co, the diamagnetic peaks corresponding to the starting $\mathbf{U^{VI}}$ disappear and 9 new paramagnetically shifted resonances appear with chemical shifts ranging from ca. 5.5 ppm to –8.0 ppm (Figure S9). And, we found the effective magnetic moment (μ_{eff}) of $\mathbf{U^{V}}$ in d_3-MeCN using Evans method to be 2.1 μ_B (See SI, pp. S27-S28), consistent with the U(V) oxidation state and prior measurements on the $5f^1$ UO_2^+ cation.[33,34] Also in accord with the expected chemical composition of $\mathbf{U^{V}}$ as a salt of the reduced uranyl complex and decamethylcobaltocenium, $[Cp^*_2Co]^+$, CV data collected for synthesized and isolated $\mathbf{U^{V}}$ revealed two quasi-reversible reduction feature with $E_{1/2}$ = –1.55 V and –1.91 V vs. $Fc^{+/0}$ in MeCN electrolyte, corresponding respectively to the $U^{VI/V}$ and $Co^{III/II}$ redox couples (Figures S29-S31). Taken together, these observations made in d_3-MeCN are consistent with clean, stoichiometric reduction of the parent $\mathbf{U^{VI}}$ complex in this solvent.

Next, we targeted preparation of $\mathbf{U^{V}B_1}$ and $\mathbf{U^{V}B_2}$. Addition of 1 or 2 equiv. of BPh_3 to $\mathbf{U^{V}}$ (generated *in situ* from $\mathbf{U^{VI}}$) resulted in a rapid color change from deep blue to wine red for the formation of $\mathbf{U^{V}B_1}$ and to light orange for $\mathbf{U^{V}B_2}$.[35] These colors persisted in the solid forms of the products that could be obtained by removal of solvent *in vacuo*. ^{1}H NMR of both borylated derivates showed the expected $[Cp^*_2Co]^+$ peak at ca. 1.70 ppm (Figures S14 and S15) and paramagnetically shifted ligand resonances in each case (Figures S16 and S17), consistent with maintenance of the paramagnetic U(V) oxidation state. All resonances associated with the $\mathbf{U^{V}}$ starting material are also lost upon addition of BPh_3 as expected.

However, in all attempts made at preparation and isolation of both $\mathbf{U^{V}B_1}$ and $\mathbf{U^{V}B_2}$ as solids, ^{1}H NMR spectra revealed additional peaks corresponding to generation of $\mathbf{U^{VI}}$ upon addition of BPh_3 (Figures S18 and S19). We were initially puzzled as to the origin of the $\mathbf{U^{VI}}$ material generated under these conditions, as clean reactivity was obtained in spectrochemical work as described above. Evidence we have assembled suggests that disproportionation reactivity becomes accessible in this system when the concentration of uranium is increased, as is necessary for synthetic work (explored here over the range of 5-20 mM). Both CV and UV-vis experiments were performed at much more dilute conditions (generally, 0.1-2 mM), giving an estimated possible acceleration in rate of up to 40,000x across our full range of studies.

Close inspection of our NMR spectra revealed that, under conditions aimed at preparation of $\mathbf{U^{V}B_1}$, resonances corresponding to $\mathbf{U^{V}B_2}$ were observable; this agrees with our CV experiments as well as computational results, as both $\mathbf{U^{V}B_1}$ and $\mathbf{U^{V}B_2}$ can form in the solution at moderate ratios of BPh_3 (due to the exergonic nature of the borylation reactions and, we anticipate, imperfect efficiency of solution stirring upon addition of the borane) making the chemical formation of $\mathbf{U^{V}B_1}$ unselective. Generation of $\mathbf{U^{V}B_2}$ under conditions where 1 eq. of BPh_3 has been added to the solution results in build-up of free $\mathbf{U^{V}}$ in the solution. However, the barrier to electron transfer from $\mathbf{U^{V}}$ to $\mathbf{U^{V}B_2}$ is modest—only 5.7 kcal mol^{-1} on the basis of the electrochemical data. Consequently, we hypothesize that electron transfer to form $\mathbf{U^{VI}}$ and $\mathbf{U^{IV}B_2}$ can occur, providing a pathway to the $\mathbf{U^{VI}}$ observed by ^{1}H NMR. At this stage, the fate of the $\mathbf{U^{IV}B_2}$ generated under these conditions is unclear, but we can implicate decomposition and/or precipitation as plausible on the basis of the limited reversibility of the CV data associated with generation of $\mathbf{U^{IV}B_2}$ and a lack of ^{1}H NMR resonances attributable to this species.[36]

To support our hypothesis that redox between $\mathbf{U^{V}}$ and $\mathbf{U^{V}B_2}$ impacts our system, we carried out a time-dependent study of the formation of $\mathbf{U^{VI}}$ under synthetic conditions, using ^{1}H NMR at 30 min intervals. An initial control experiment showed that $\mathbf{U^{V}}$ is stable in d_3-MeCN out to 24 h in the absence of BPh_3, while experiments where $\mathbf{U^{V}}$ was mixed with 1 or 2 equiv. of BPh_3 showed formation of

$\mathbf{U^{VI}}$ as noted above (Figures S20-S22). At 30 min after mixing, approximately 2x as much $\mathbf{U^{VI}}$ had been produced when 1 equiv. of BPh_3 had been added in comparison to the amount when 2 equiv. had been added, consistent with the greater likelihood for co-generation of $\mathbf{U^{V}}$ with $\mathbf{U^{V}B_2}$ under the former conditions.

To our surprise, however, $\mathbf{U^{VI}}$ continued to form even after the initial 30 min; the rate of this U(VI) production is clearly greater in the case of addition of 1 equiv. of BPh_3. This observation suggests that the $\mathbf{U^{V}B_1}$ complex may undergo disproportionation behavior via "ligand exchange" or loss of BPh_3 from the oxo moieties, leading to *in situ* production of additional $\mathbf{U^{V}}$ and subsequent electron transfer. The same behavior may be postulated for $\mathbf{U^{V}B_2}$ on the basis of a similar (although minor) increase in $\mathbf{U^{VI}}$ generation for conditions where 2 equiv. of BPh_3 were added.

Spectroscopic Evidence for the U(V) Oxidation State

On the basis of the work presented so far, the $\mathbf{U^{V}}$, $\mathbf{U^{V}B_1}$, and $\mathbf{U^{V}B_2}$ species should feature uranium centers having the +5 formal oxidation state. To provide support for this assignment and firmly connect the electrochemical reactivity patterns with generation of *bona fide* U(V), we carried out further spectroscopic work. The infrared spectrum of powdered $\mathbf{U^{VI}}$ revealed a band attributable to the asymmetric stretch of the uranyl group (ν_{asym}) at 883 cm^{-1} (Figures S60 and S61); this band disappeared upon generation of $\mathbf{U^{V}}$, consistent with the anticipated reduction of the uranium center (Figures S62 and S63). Inspection of the spectrum of $\mathbf{U^{V}}$ at energies ca. 125 cm^{-1} lower than the ν_{asym} for $\mathbf{U^{VI}}$,[13] however, did not reveal an obvious feature for the corresponding asymmetric stretch of $\mathbf{U^{V}}$. However, there are significant features near 758 cm^{-1} found in the spectra of both $\mathbf{U^{VI}}$ and $\mathbf{U^{V}}$, suggesting that the asymmetric dioxo stretch is obscured by ligand-derived features in $\mathbf{U^{V}}$.

Stronger support for the presence of U(V) came from near-infrared (NIR) spectroscopic studies. Prior work from Hayton and co-workers,[14,15] Arnold and co-workers,[19] and others[28,37] have demonstrated that U(V) centers tend to display transitions in the near-infrared region that can be assigned to Laporte-forbidden *5f* to *5f* transitions. In our case, the spectrum of $\mathbf{U^{V}}$ in MeCN revealed a main transition centered at 7,215 cm^{-1} with $\varepsilon \approx 77$ M^{-1} cm^{-1}, along with a minor observable shoulder on the low energy side of the main transition (Figure 4, panel a and Figure S65). This profile is consistent with U(V).

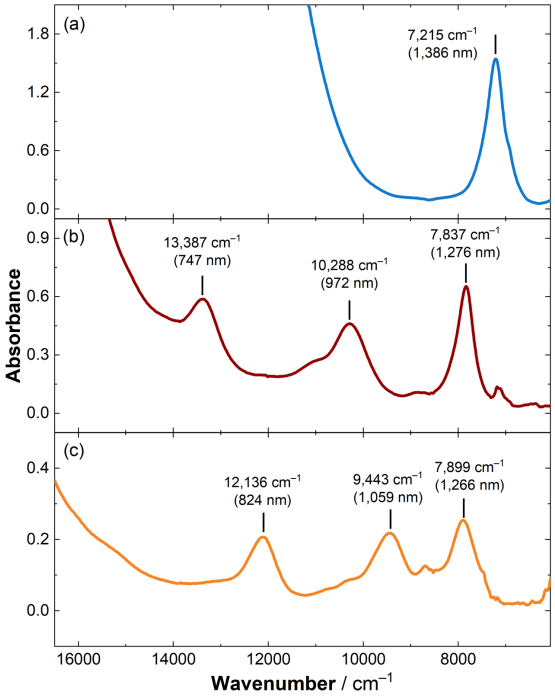

Figure 4. Near-IR spectral spectra of *in situ* generated $\mathbf{U^{V}}$ (panel a), $\mathbf{U^{V}B_1}$ (panel b), and $\mathbf{U^{V}B_2}$ (panel c). The concentration of $\mathbf{U^{VI}}$ used to generate all species *in situ* was 20 mM.

As the formal U(V) oxidation state should be maintained upon borylation of the oxo moieties, we also carried out NIR studies on *in situ*-generated samples of the borylated species. Upon addition of 1 or 2 equiv. of BPh_3 to $\mathbf{U^{V}}$ to generate $\mathbf{U^{V}B_1}$ and $\mathbf{U^{V}B_2}$, respectively, spectral changes were observed in the NIR region. The solution containing $\mathbf{U^{V}B_1}$ displayed transitions at 13,387 cm^{-1}, 10,288 cm^{-1}, and 7,837 cm^{-1} (Figure 4, panel b and Figure S66) while the solution containing $\mathbf{U^{V}B_2}$ displayed transitions at 12,136 cm^{-1}, 9,443 cm^{-1}, and 7,899 cm^{-1} (Figure 4, panel c and Figure S67). Appealingly, prior NIR work on U(V) species functionalized with $B(C_6F_5)_3$ has revealed that multiple transitions can be observable with such species. We anticipate that the similar composition of our complexes gives rise to the similarities between these prior spectra and our own. And we emphasize that the clear distinction between the spectra of $\mathbf{U^{V}B_1}$ and $\mathbf{U^{V}B_2}$ in the NIR region suggests that these *in situ* generated species can be generated in high yields, in line with evidence from the electrochemical work as well as NMR (*vide supra*). The shift of the two higher energy bands for $\mathbf{U^{V}B_1}$ to $\mathbf{U^{V}B_2}$ to lower energies could be consistent with diminished π-donation from the oxo ligands upon binding of BPh_3.

We also attempted X-band electron paramagnetic resonance (EPR) studies to further probe the formation of the U(V) species in solution. We prepared the U(V) complexes with *in situ* mixing methods similar to those described above. However, the 10 K EPR spectra of the frozen reaction solutions showed an absence of any appreciable signal in all cases (Figure S75). The observation that the complexes are EPR silent in frozen solution could suggest the presence of magnetic exchange interactions between U(V) centers in the frozen solutions.[38] Therefore, we anticipate that our complexes undergo aggregation at low temperature, leading to loss of the anticipated U(V) signals and observation of only extremely weak organic radical signals associated with sample contamination and/or minor decomposition.

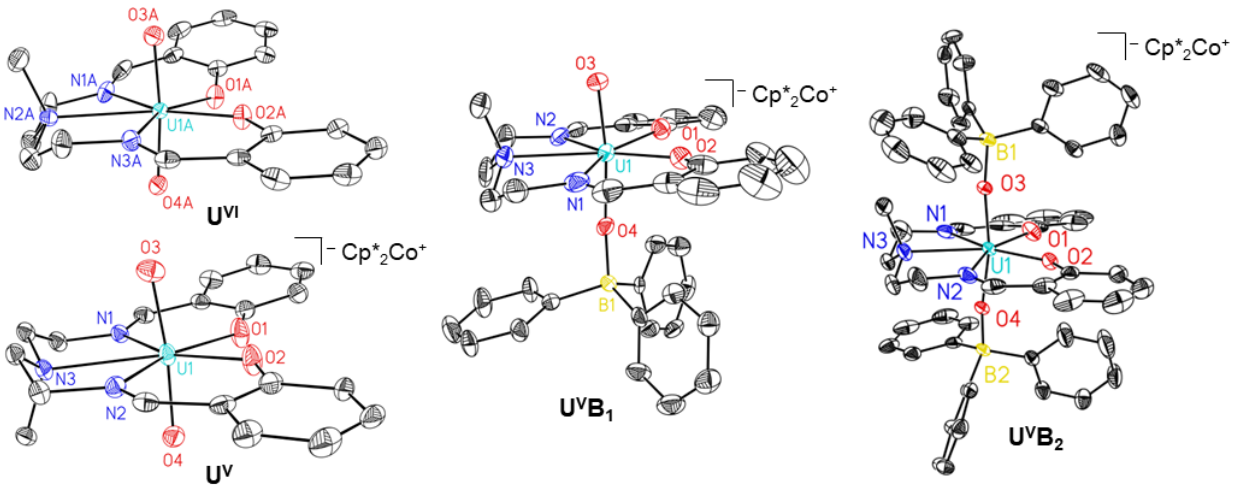

Figure 5. Solid-state structure (XRD) of $\mathbf{U^{VI}}$, $\mathbf{U^{V}}$, $\mathbf{U^{V}B_1}$, and $\mathbf{U^{V}B_2}$. All hydrogen atoms, co-crystallized solvent molecules, cobaltocenium countercations, and minor components of disorder are omitted for clarity. Displacement ellipsoids are shown at 50% probability level for complex $\mathbf{U^{VI}}$, $\mathbf{U^{V}B_1}$, and $\mathbf{U^{V}B_2}$, and at 20% probability level for complex $\mathbf{U^{V}}$.

X-ray Diffraction Studies

Encouraged by our isolation of $\mathbf{U^{VI}}$ and $\mathbf{U^{V}}$ as clean powdered samples, and by our observations that $\mathbf{U^{V}B_1}$ and $\mathbf{U^{V}B_2}$ could be cleanly generated in solution, we pursued structures of these complexes from single-crystal X-ray diffraction (XRD) analysis. Suitable crystals of $\mathbf{U^{VI}}$ were grown by diffusion of Et_2O into a MeCN solution. The resulting solid-state structure confirms that the first coordination sphere around uranium contains the $\kappa^{5\text{-}Me}$saldien scaffold and two terminal oxo ligands. The average U–O_{oxo} distance of 1.789(3) Å is consistent with U(VI) oxidation state, lying in the typical range of values for uranyl complexes.[7]

Blue crystals of $\mathbf{U^{V}}$ were also obtained by vapor diffusion of Et_2O into a solution of the complex in MeCN. The ligands found in the first coordination sphere about the uranium center in $\mathbf{U^{V}}$ are identical to those found in $\mathbf{U^{VI}}$, in accord with transfer of only $1e^-$ to form this species from $\mathbf{U^{VI}}$. Notably, however, the average U–O_{oxo} bond distance is elongated to 1.850(7) Å; this elongation of 0.061 Å is consistent with generation of the U(V) oxidation state. The U–$O_{phenoxide}$ distances are also elongated in $\mathbf{U^{V}}$, consistent with generation of a more electron-rich uranium center upon reduction (Table 1). On the other hand, the C–N_{imine} distance of one of the imine bonds is 0.015 Å greater than that of the $\mathbf{U^{VI}}$ complex; this elongation may be attributed to the participation of the ligand in the reduction process, leading to a partial ligand radical character for $\mathbf{U^{V}}$. However, this increase is smaller than the change observed in U–O_{oxo}, which suggests that the majority of electron density remains localized on the uranium center; this observation aligns with the findings from the computational studies (*vide infra*).

NMR spectra of *in situ* generated $\mathbf{U^{V}B_1}$ and $\mathbf{U^{V}B_2}$ support that the dominant species in the solution are desired borylated species, even though some disproportionation occurs at higher concentrations leading to unclean chemical reactivity. By taking advantage of the change in concentration during vapor diffusion and starting with dilute solutions, single crystals were grown successfully using a MeCN-Et_2O solvent system for $\mathbf{U^{V}B_1}$ and a CH_2Cl_2-Et_2O system for $\mathbf{U^{V}B_2}$. Both structures demonstrate that the first coordination sphere around the uranium center containing the $\kappa^{5\text{-}Me}$saldien scaffold remained intact upon functionalization of $\mathbf{U^{V}}$ with BPh_3.

The structure of $\mathbf{U^{V}B_1}$ reveals coordination of BPh_3 to one of the oxo ligands, resulting in the elongation of the U–O_{oxo} to 1.973(6) Å while the other oxo ligand retains a similar bond length, 1.850(6) Å, as those observed for the U–O_{oxo} distances in $\mathbf{U^{V}}$. This is consistent with functionalization of only one oxo ligand, while maintaining the formal U(V) oxidation state of the uranium center. In the solid-state structure of $\mathbf{U^{V}B_2}$ both uranyl oxo ligands are coordinated by borane equivalents, resulting in an overall elongation of both U–O_{oxo} bonds to 1.952(2)/1.959(2) Å. This corresponds to a U–O lengthening of 0.167 Å compared to $\mathbf{U^{VI}}$, which featured values for these bonds of 1.784(3)/1.793(3) Å. Such elongation could be expected as the interaction of Lewis acidic borane with electron-rich oxo ligand should weaken the interaction between the oxo moiety and uranium center, causing the uranium to become more electron-deficient. For comparison, a recently reported bis-borylated complex featuring $B(C_6F_5)_3$ that was reported by Arnold and Love[19] featured a change in U–O_{oxo} bond distance of 0.155 Å relative to an analogous U(VI) complex. The high degree of activation in our system could be attributable to its overall negative charge, or perhaps to unique features arising from use of BPh_3.

In line with the above changes, the average U–$O_{phenoxide}$ distance shortens upon mono-borylation from 2.368(7) Å in $\mathbf{U^{V}}$ to 2.282(6) Å in $\mathbf{U^{V}B_1}$. This observation aligns with the uranium center becoming more electron-deficient following oxo functionalization, a process which drives a greater pull of the electropositive uranium center on the electron density associated with the phenoxide oxygen atoms. This trend continues upon di-functionalization, as the structure of $\mathbf{U^{V}B_2}$ features an average U–$O_{phenoxide}$ distance of 2.195(2) Å. And, finally, there is an overall decrease in the $O3_{oxo}$–U–$O4_{oxo}$ angle from $\mathbf{U^{VI}}$ to $\mathbf{U^{V}B_2}$ of 6.3°, indicating a change in the geometry of the uranyl ion from linear to slightly bent; this is in accordance with the loss of "*yl*" character in the oxo ligands upon activation, consistent with the preference for σ-only bonding between U and O upon oxo borylation.

Table 1. Comparison of selected structural parameters of U^{VI}, U^{V}, $U^{V}B_1$, and $U^{V}B_2$ from X-ray diffraction analysis and the DFT calculations.

	U^{VI}		U^{V}		$U^{V}B_1$		$U^{V}B_2$	
	XRD	DFT [d]	XRD	DFT [d]	XRD	DFT [d]	XRD	DFT [d]
$U–O1_{phenoxide}$ (Å)	2.219(3)[a]	2.234	2.366(7)	2.363	2.273(6)	2.288	2.186(3)	2.210
$U–O2_{phenoxide}$ (Å)	2.226(3)[a]	2.238	2.370(6)	2.374	2.291(6)	2.301	2.204(2)	2.211
$U–O_{phenoxide}$ (avg) (Å)[b]	2.223(3)	2.236	2.368(7)	2.369	2.282(6)	2.295	2.195(2)	2.211
$U–O3_{oxo}$ (Å)	1.784(3)[a]	1.775	1.853(7)	1.822	1.850(6)	1.816	1.952(2)	1.952
$U–O4_{oxo}$ (Å)	1.793(3)[a]	1.777	1.847(7)	1.821	1.973(6)	1.968	1.959(2)	1.956
$U–O_{oxo}$ (avg) (Å)[c]	1.789(3)	1.776	1.850(7)	1.822	-	-	1.956(2)	1.954
$N1–C1_{imine}$ (Å)	1.290(6)[a]	1.286	1.305(10)	1.288	1.291(14)	1.283	1.290(7)	1.283
$N2–C14_{imine}$ (Å)	1.287(5)[a]	1.284	1.292(10)	1.285	1.269(14)	1.283	1.284(5)	1.283
$O3_{oxo}–B$ (Å)	-	-	-	-	-	-	1.545(5)	1.555
$O4_{oxo}–B$ (Å)	-	-	-	-	1.556(11)	1.533	1.551(5)	1.558
$O3_{oxo}–U–O4_{oxo}$ (deg)	175.6(1)[a]	172.5	173.1(3)	173.2	172.8(3)	171.6	169.3(1)	171.3

[a] Average values of parameters for $\mathbf{U^{VI}}$ were calculated as the arithmetic mean of the relevant values for the two independent molecules of $\mathbf{U^{VI}}$ in the asymmetric unit. Stated e.s.d.'s on distances were taken as the largest of the individual values in the refined data for the independent molecular species. [b] Defined as the average of the interatomic distances between the uranium center and the O-atoms of the bridging phenoxide moieties. [c] Defined as the average of the interatomic distances between the uranium center and the two oxygen atoms of the oxo ligands. [d] Calculated using the B3PW91/SARC-ZORA/ZORA-def2-TZVP level of theory.

Computational Studies

Geometries. Calculations with density functional theory (DFT) were used to probe the electronic structures of the isolated complexes as well as the proposed electrogenerated species, to compare their properties, and to aid in understanding the overall energetics of the electrochemical reactivity encountered in this work. In large systems of the type studied here, searching for the global minimum structure is challenging due to the large number of degrees of freedom, resulting in the possible existence of local minima. To determine the putative global energy minima and the corresponding electronic stabilization of the complexes $\mathbf{U^{VI}}$, $\mathbf{U^{V}}$, $\mathbf{U^{V}B_1}$, and $\mathbf{U^{V}B_2}$, we employed NWPEsSe, an adaptive-learning global optimizer based on the concept of an artificial bee colony (see p. S59 for details).[39] The DFT exchange-correlation functional B3PW9140[41] was employed, along with the relativistic basis sets SARC/ZORA-TZVP.[42,43](see p. S63 for details).

The geometric parameters for $\mathbf{U^{VI}}$, $\mathbf{U^{V}}$, $\mathbf{U^{V}B_1}$, and $\mathbf{U^{V}B_2}$ were first compared to their corresponding experimental values (see Table 1). Generally speaking, the values show reasonable agreement, revealing an average difference of approximately 0.007 Å between the experimental and calculated values. This result suggests the chosen theoretical approach and level of theory are appropriate to reproduce the properties of the complexes.

The bond length of $U–O_{oxo}$ in $\mathbf{U^{VI}}$ was calculated to be 2.236 Å, with elongation to 2.369 Å in $\mathbf{U^{V}}$ due to charge transfer to the uranium center and reduction in formal oxidation state. The addition of BPh_3 causes an increase in the length of the U–O bonds in both $\mathbf{U^{V}B_1}$ and $\mathbf{U^{V}B_2}$, due to sharing of electron density from oxygen with the boron atoms in the added borane(s). The terminal $U–O_{oxo}$ bond length was observed to be shorter (by computation and by XRD) in $\mathbf{U^{V}B_1}$ compared to the corresponding bonds in $\mathbf{U^{V}B_2}$ between the oxo-derived oxygens and uranium center, suggesting a higher strength for this interaction when borane is not present.

The strength of the $O_{oxo}–B$ bond was assessed by calculating the bond dissociation energy, obtained here by taking the difference between the total enthalpy of the complex and the sum of the energies of the two relevant molecular fragments ($\mathbf{U^{V}}$ and the MeCN adduct of BPh_3). The bond dissociation energy values reveal that the O_{oxo}-B bond is stronger in $\mathbf{U^{V}B_1}$, measuring 0.75 eV, compared to $\mathbf{U^{V}B_2}$, which has a bond dissociation energy of 0.59 eV (Table S4).

Energetics. The Gibbs free energies, ΔG, of the electrochemical oxo-activation cycle are presented in Scheme 3. Each structure was optimized at the same level of theory; frequency calculations confirmed that the optimized structures were at a minimum in each case. The ΔG was then calculated as the difference between the energies of the products and reactants in each reaction (see Table S6 for details). The first step of the reaction sequence involves a redox reaction where an electron is transferred from Cp^*_2Co to $\mathbf{U^{VI}}$, resulting in the formation of $[\mathbf{U^{V}}]^-$ and $Cp^*_2Co^+$. Theory suggests that this reaction is quite exothermic, with $\Delta G = -1.54$ eV in the gas phase. This is in accord with the clean reactivity corresponding to $\mathbf{U^{V}}$ generation observed in the experimental work.

Regarding the solution structure of the BPh_3 electrophile, experimental infrared spectra (Figures S58 and S59) indicate that BPh_3 coordinates an equivalent of MeCN in solution. This means that engagement in bonding with $\mathbf{U^{V}}$ follows loss of this interaction. Computational analysis confirmed the existence of the MeCN-BPh_3 adduct with a B–N bond length of 1.602 Å. During the second step of the cycle, we can confirm that the B–N bond is broken upon exposure of the adduct to $\mathbf{U^{V}}$, allowing BPh_3 to coordinate with the uranyl oxo ligand. The ΔG value for this overall reaction was calculated to be –0.53 eV, consistent with observation of generation of $\mathbf{U^{V}B_1}$ in the electrochemical work. Similarly, BPh_3 coordination to form $\mathbf{U^{V}B_2}$ was calculated to be exergonic by $\Delta G = -0.51$ eV, again consistent with the confirmation of formation of this species in the experimental work under electrochemical conditions.

Computational analysis was also conducted on the putative oxidized forms of the borylated species $\mathbf{U^{VI}B_1}$ and $\mathbf{U^{VI}B_2}$ that were

found to be accessible by electrogeneration in this work (Scheme 3). The results show that formation of $\mathbf{U^{VI}B_1}$ is endergonic by 1.90 eV compared to $\mathbf{U^{V}B_1}$ (Table S6). Similarly, $\mathbf{U^{VI}B_2}$ was determined to be energetically higher than $\mathbf{U^{V}B_2}$ by 1.24 eV. Furthermore, the bond dissociation energies of the O_{oxo}-B bonds in the $\mathbf{U^{VI}B_1}$ and $\mathbf{U^{VI}B_2}$ species are close to zero (Table S4), confirming the experimental observation that BPh_3 does not coordinate to the uranyl oxo ligand in the U(VI) oxidation state.

Reactivity parameters. The reactivity of compounds (including actinide-containing species) can be inferred by evaluating the energy levels of the HOMO and LUMO and determining the energy gap between them, ΔE_{gap}.[44] $\mathbf{U^{VI}}$ exhibits the largest ΔE_{gap} of 1.7 eV, as shown in Table S5. The complexes $\mathbf{U^{V}}$, $\mathbf{U^{V}B_1}$, and $\mathbf{U^{V}B_2}$ are categorized as open-shell compounds, with the highest orbitals being singly occupied molecular orbitals (SOMOs). The reduction in oxidation state in these complexes is reflected by relatively small values of ΔE_{gap}, especially in the $\mathbf{U^{V}}$, where ΔE_{gap} is only 0.3 eV, indicating an increased likelihood of reactivity from these complexes that is consistent with our experimental observations.

The introduction of BPh_3 has an additional influence on the energy levels of the HOMO and LUMO. In $\mathbf{U^{V}B_1}$, the ΔE_{gap} is 0.5 eV, while in $\mathbf{U^{V}B_2}$, it is 0.6 eV. Consequently, these complexes can be ranked in their order of stability as $\mathbf{U^{VI}} > \mathbf{U^{V}B_2} > \mathbf{U^{V}B_1} > \mathbf{U^{V}}$. This overall profile is consistent with our experimental observations in that $\mathbf{U^{VI}}$ is quite stable, but the formation of $\mathbf{U^{V}}$ enables reactivity leading to the mono- and di-functionalized species.

However, the energies of the HOMO/SOMO and LUMO orbitals suggest a degree of degeneracy. In all $\mathbf{U^{VI}}$, $\mathbf{U^{V}}$ and $\mathbf{U^{V}B_1}$, the HOMO/SOMO show significant contribution from the uranyl and extended ligand, while $\mathbf{U^{V}B_2}$ mostly exhibits contributions from the core uranyl-derived $[UO_2]$ moiety (Figure S82). The LUMO of $\mathbf{U^{VI}}$ and $\mathbf{U^{V}B_2}$ has mostly contribution from the uranyl unit, while in $\mathbf{U^{V}}$ and $\mathbf{U^{V}B_1}$, the LUMO extends into the ligand. Although the molecular orbital picture is useful for understanding the extent of mixing of the atomic orbitals, it becomes less intuitive for understanding the bonding patterns, which tend to be more localized; stated another way, molecular orbitals are naturally delocalized when extended ligands are present. For this reason, we next performed a natural bond orbital (NBO) analysis to investigate the bonding in these systems.

NBO charge and bond order analysis. Natural orbitals (NOs) are eigen solutions of the first-order reduced electron-density operator and correspond to maximum occupancies.[45,46] Thus, natural bond orbitals (NBOs) are derived from a localization procedure and, as such, are confined to fewer atomic centers, can better describe the bonding patterns and charge transfer within a molecular system, and are more useful for translating electronic structure changes into chemical insights.[47,48] For example, a second-order perturbation theory analysis can help quantify the charge transfer between sub-molecular units.[49]

The natural charges of selected atoms are provided in Table 2 (and Figure S83). Upon reduction of $\mathbf{U^{VI}}$ to $\mathbf{U^{V}}$, the NBO charge analysis reveals a slight difference in charge between the species, with $\mathbf{U^{VI}}$ having a charge of +1.603 |e| and $\mathbf{U^{V}}$ having a charge of +1.518 |e|, emphasizing the difference between the formal oxidation state and formal charge in this case. Consequently, the natural charges at the oxygens in the uranyl moiety in $\mathbf{U^{VI}}$ are lower, averaging –0.534|e| compared to –0.713 |e| in $\mathbf{U^{V}}$. This is consistent with increased oxo-centered basicity in $\mathbf{U^{V}}$.

Upon inspecting the U–O_{oxo} bonding in $\mathbf{U^{VI}}$, the NBOs for the U–O_{oxo} σ-bond show mostly $5f_{z^3}$ character (see Figure 7, panel a and Figure S85). This behavior closely resembles the natural orbitals present in the isolated uranyl ion (Figure S84). Second-order perturbation analysis of the Fock matrix in the NBO basis[50] allows further quantification of the bonding interaction energies. In principle, larger interactions energies are indicative of the stronger integrations between the atoms and charge transfer. This analysis reveals strong electron donation between the donor (bonding) and acceptor (anti-bonding) orbitals for U–$O3_{oxo}$ and U–$O4_{oxo}$ moieties. Specifically, there is a significant donation from U–$O3_{oxo}$ to the anti-bonding of U–$O4_{oxo}$, and vice versa, with interaction energies of 2.4 eV (55.69 kcal/mol) and 1.7 eV (29.22 kcal/mol), respectively. The analysis is also consistent with the existence of a triple bond between U and the O_{oxo} atoms in $\mathbf{U^{VI}}$.[51]

Table 2. Natural charges for selected atoms in $\mathbf{U^{VI}}$, $\mathbf{U^{V}}$, $\mathbf{U^{V}B_1}$, and $\mathbf{U^{V}B_2}$ complexes in [e].

	$\mathbf{U^{VI}}$	$\mathbf{U^{V}}$	$\mathbf{U^{V}B_1}$	$\mathbf{U^{V}B_2}$
U	1.603	1.518	1.705	2.201
$O3_{oxo}$	–0.534	–0.713	–0.767	–0.850
$O4_{oxo}$	–0.537	–0.714	–0.716	–0.849
$N1_{imine}$	–0.439	–0.437	–0.434	–0.482
$N2_{imine}$	–0.428	–0.427	–0.429	–0.481
$C1_{imine}$	0.182	0.155	0.154	0.184
$C14_{imine}$	0.178	0.148	0.173	0.183
$N3_{amine}$	–0.389	–0.387	–0.395	–0.445
$O1_{phenoxide}$	–0.596	–0.615	–0.630	–0.711
$O2_{phenoxide}$	–0.595	–0.617	–0.627	–0.712
B1	-	-	0.507	0.507
B2	-	-	-	0.212

A similar NBO picture emerges in the reduced complex $\mathbf{U^{V}}$ (Figure 7, panel b and Figure S86); however, the extent of the charge transfer is diminished compared to $\mathbf{U^{VI}}$. Here, the electron donation from U–$O4_{oxo}$ to the anti-bonding acceptor U–$O3_{oxo}$ is approximately 1.1 eV (ca. 25 kcal/mol) compared to the $\mathbf{U^{VI}}$ system. Similarly, the donation from U–$O3_{oxo}$ to the U–$O4_{oxo}$ anti-bonding acceptor is also decreased by about 0.5 eV (ca. 12 kcal/mol). These findings further support overall weakening of the U–O bonding in $\mathbf{U^{V}}$ and increased basicity of the reduced form, $\mathbf{U^{V}}$.

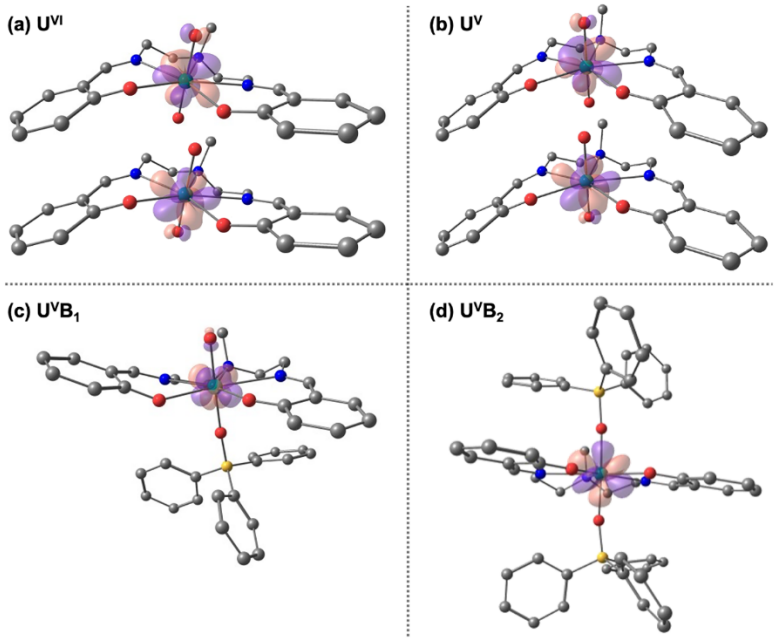

Figure 7. Representative natural bond orbitals (NBOs) associated with bonding in the $[UO_2]$-derived cores of the complexes reported in this work. Panel (a) for $\mathbf{U^{VI}}$ and panel (b) for $\mathbf{U^{V}}$ show the U–$O3_{oxo}$ and U–$O4_{oxo}$ NBOs in the upper and lower structures, respectively. Panel (c) shows the U–$O3_{oxo}$ bond orbitals in $\mathbf{U^{V}B_1}$. Panel (d) shows the uranium-only natural orbital in $\mathbf{U^{V}B_2}$. Hydrogens are omitted for clarity. Images generated for 0.15 isovalue. For more details, see SI p. S65-S75.

The $\mathbf{U^{V}B_1}$ structure results from the addition of 1 equiv. BPh_3 and functionalization of one U–O_{oxo} moiety (Figure 7, panel c; Figures S87 and S88). NBO analysis revealed that the lone pair of the $O4_{oxo}$ atom donates electrons to the anti-bonding acceptor U–$O3_{oxo}$, resulting in an interaction energy of 0.4 eV. Additionally, the lone pair of $O4_{oxo}$ atom donates electron density to the vacant orbital of the boron atom. However, in the $\mathbf{U^{V}B_1}$ system, no charge transfer between the bonding/anti-bonding orbitals of U–$O3_{oxo}$ and U-bonds is observed. As expected, the inclusion of BPh_3 leads to an increase of the U–$O4_{oxo}$ bond length and an increase in the uranium natural charge (+1.71 |e|). Interestingly, the natural charges of the $O4_{oxo}$ do not change significantly before/after this process (–0.7 |e| for both $\mathbf{U^{V}}$ and $\mathbf{U^{V}B_1}$) despite binding to the B1 atom; however, the $O3_{oxo}$ atom shows an increase in natural charges to –0.77 |e|. Overall, the addition of BPh_3 to form $\mathbf{U^{V}B_1}$ can be concluded to result in electron density increase towards U–$O3_{oxo}$ bond, meaning that the terminal oxo moiety is predicted to retain high enough Lewis basicity that it can undergo borylation as well when sufficient exogeneous borane is available.

Upon addition of the second BPh_3 equivalent and formation of $\mathbf{U^{V}B_2}$, there is a further shift in the electron density away from the uranium center (Figure 7, panel d; Figures S89 and S90). The natural charge of uranium now increases to +2.20 |e|, and no back-bonding interactions are observed between the bonding/anti-bonding orbitals in the $[UO_2]$-derived moiety. The natural charges of both O_{oxo} atoms are increased to –0.85 |e|, consistent with the higher charge on the U atom. Similar to $\mathbf{U^{V}B_1}$, the lone pair on the $O4_{oxo}$ donates electron density to the lone valence orbital of B1 atom, with an interaction energy of 5.6 eV. $O3_{oxo}$ donates to the B2 atom with a similar interaction energy of 5.4 eV. As a result of these interactions, both $\mathbf{U^{V}B_1}$ and $\mathbf{U^{V}B_2}$ complexes are stabilized, making them energetically more favorable than the related open shell system present in the $\mathbf{U^{V}}$ species.

Discussion

In this work, we set out to explore the use of electrochemical methods for activation and functionalization of the uranyl ion, and to compare their use with traditional chemical reagents. In our approach, we substituted a polarized electrode as a source of reducing equivalents in place of a chemical reductant, enabling us to electrogenerate the formally uranium(V) form of a model uranyl-containing starting material, and then use electrochemical signatures to track the products of reactivity of the uranium(V) complex with a model mild electrophile, BPh_3. To the best of our knowledge, such molecular reactivity of a well-defined set of coordination complexes has not been initiated or tracked electrochemically, adding molecular insights into electrochemical routes for uranium processing. In context, this electro-activation strategy is related to ongoing work in the field on molten salt electrolysis of used nuclear fuels, an up-and-coming strategy for handling, processing, and recycling of actinide materials.[52,53] Considering all this, we anticipate that further development of systems for interrogating electro-induced actinide reactivity could be attractive.

In this work, we substituted the electrophile BPh_3 in place of its more commonly investigated analogue $B(C_6F_5)_3$. This represents a substantial change, as the fluorination of the former reagent makes it a significantly stronger Lewis acid than the latter. However, based on the structural data reported here, we can conclude that BPh_3 can facilitate oxo activation much like $B(C_6F_5)_3$. In this context, our new BPh_3 adducts feature quite long U–O_{oxo} bonds of 1.96-1.97 Å (Table 1), in line with a high degree of loss of the multiple bond character between U and the former oxo ligands in these species. Further exploration of oxo activation with weaker Lewis acids and more sustainable reagents appears called for on the basis of this work, as strongly electrophilic reagents may not be required. An attractive aspect of the use of weaker electrophiles is the avoidance of direct

electron transfer to these species under functional conditions; this mode of reactivity was virtually completely avoided here as BPh_3 direct reduction at electrodes does not compete for charge transfer with the uranium species in our study.

In our view, this work opens the attractive possibility of accessing meta-stable or transient uranium-containing species for study with electrochemical methods, an approach that will complement prior work in chemical conversion of uranyl species to more reactive forms. As noted here, our complexes are accessible cleanly under electrochemical conditions but, in some cases, could not be isolated in pure form due to concentration-dependent speciation chemistry. Similarly, we note that we have quantified potentials associated with generation of various species in this work, and assembled qualitative evidence associated with observation of new reaction pathways. An additional opportunity which we are now pursuing is quantification of the rates of the various chemical reactions involved in uranyl oxo activation; electroanalytical methods appear well poised to allow access to quantitative data in this realm, a particularly attractive prospect for understanding the properties of key transient intermediates identified through this work.

Conclusions

In conclusion, we have described here an electrochemical approach to generating and characterizing species involved in uranyl activation and functionalization. The use of electrochemical methods to electrogenerate reactive uranium complexes appears to be an attractive opportunity for further development, as some cross-reactivity that can affect conventional chemical systems was avoided here through the use of electrochemical methods. Computational studies of the electronic structures and NBO analysis revealed that the addition of BPh_3 stabilizes the open shell reduced complexes compared to the original $\mathbf{U^V}$ complex, providing support for the role of this electrophile in the reactivity scheme. In particular, the binding of BPh_3 disrupts essential back donor effects involved in the U–O bonds in the uranyl moiety, leading to weakening and activation of these bonds as confirmed in the structures of the borylated products. These observations highlight the power of synergistic chemical, electrochemical, and theoretical work in approaching future studies of reactive actinide-containing coordination complexes.

ASSOCIATED CONTENT

Experimental details; synthesis and characterization of compounds used in this study; NMR spectra; crystallographic details; electronic absorption spectra; infrared spectra; near-infrared spectra; electro-chemical data
Crystal data
Cartesian coordinates from single-crystal XRD studies

AUTHOR INFORMATION

Corresponding Authors

James D. Blakemore – *Department of Chemistry, University of Kansas, Lawrence, Kansas 66045, United States*; orcid.org/0000-0003-4172-7460; Phone: +1 (785)864-3019; Email: blakemore@ku.edu

Vassiliki-Alexandra Glezakou – *Chemical Sciences Division, Oak Ridge National Laboratory, Oak Ridge, Tennessee 37830, United States*; orcid.org/0000-0001-6028-7021; Email: glezakouva@ornl.gov

Authors

Riddhi R. Golwankar – *Department of Chemistry, University of Kansas, Lawrence, Kansas 66045, United States*; orcid.org/0000-0003-3957-7862

Małgorzata Z. Makoś – *Chemical Sciences Division, Oak Ridge National Laboratory, Oak Ridge, Tennessee 37830, United States*; orcid.org/0000-0002-6015-5608

Nathalia Cajiao – *Department of Chemistry, University of Rochester, Rochester, New York14627, United States*

Michael L. Neidig – *Department of Chemistry, University of Rochester, Rochester, New York14627, United States; Inorganic Chemistry Laboratory, Department of Chemistry, University of Oxford, Oxford OX1 3QR, United Kingdom*; orcid.org/0000-0002-2300-3867

Allen G. Oliver – *Department of Chemistry & Biochemistry, University of Notre Dame, Notre Dame, Indiana 46556, United States*; orcid.org/0000-0002-0511-1127

Cynthia S. Day – *Department of Chemistry, Wake Forest University, Winston-Salem, North Carolina 27109, United States*

Victor W. Day – *Department of Chemistry, University of Kansas, Lawrence, Kansas 66045, United States*

Author Contributions

The manuscript was written through contributions of all authors. All authors have given approval to the final version of the manuscript.

Notes

The authors declare no competing financial interest.

ACKNOWLEDGMENT

This work was supported by the U.S. Department of Energy, Office of Basic Energy Sciences through the Early Career Research Program (DE-SC0019169). V.A.G. and M.Z.M. were supported by the LDRD program at Oak Ridge National Laboratory. M.L.N. acknowledges financial support from the U.S. Department of Energy, Office of Science, Office of Basic Energy Sciences, Heavy Element Chemistry Program (DE-SC0021917). X-ray facilities at Wake Forest University were supported by the US National Science Foundation through award CHE-0234489.

REFERENCES

[1] (a) Walter, M. G.; Warren, E. L.; McKone, J. R.; Boettcher, S. W.; Mi, Q.; Santori, E. A.; Lewis, N. S., Solar Water Splitting Cells. *Chem. Rev.* **2010,** *110*, 6446-6473. (b) Bottecchia, C.; Lehnherr, D.; Lévesque, F.; Reibarkh, M.; Ji, Y.; Rodrigues, V. L.; Wang, H.; Lam, Y.-h.; Vickery, T. P.; Armstrong, B. M.; Mattern, K. A.; Stone, K.; Wismer, M. K.; Singh, A. N.; Regalado, E. L.; Maloney, K. M.; Strotman, N. A., Kilo-Scale Electrochemical Oxidation of a Thioether to a Sulfone: A Workflow for Scaling up Electrosynthesis. *Organic Proc. Res. Dev.* **2022,** *26*, 2423-2437.

(2) Bard, A. J.; Parsons, R.; Jordan, J., *Standard Potentials in Aqueous Solution*. M. Dekker: New York, 1985.

(3) Pourbaix, M. *Atlas of Electrochemical Equilibria in Aqueous Solutions*. Pergamon Press: 1966.

(4) Meinrath, G. Coordination of uranyl(VI) carbonate species in aqueous solutions. *J. Radioanal. Nucl. Chem.* **1996,** *211*, 349-362.

(5) Gibson, J. K.; Haire, R. G.; Santos, M.; Marçalo, J.; Pires de Matos, A. Oxidation studies of dipositive actinide ions, An^{2+} (An= Th, U, Np, Pu, Am) in the gas phase: Synthesis and characterization of the isolated uranyl, neptunyl, and plutonyl ions UO_2^{2+} (g), NpO_2^{2+} (g), and PuO_2^{2+} (g). *J. Phys. Chem. A* **2005**, *109*, 2768-2781.

(6) Fortier, S.; Hayton, T. W. Oxo ligand functionalization in the uranyl ion (UO_2^{2+}). *Coord. Chem. Rev.* **2010,** *254*, 197-214.

(7) Cowie, B. E.; Purkis, J. M.; Austin, J.; Love, J. B.; Arnold, P. L. Thermal and Photochemical Reduction and Functionalization Chemistry of the Uranyl Dication, $[U^{VI}O_2]^{2+}$. *Chem. Rev.* **2019**, *119*, 10595-10637.

(8) Berthet, J.-C.; Nierlich, M.; Ephritikhine, M. Complexes triflates de l'uranium. *C. R. Chim.* **2002,** *5*, 81-87.

(9) Natrajan, L.; Burdet, F.; Pécaut, J.; Mazzanti, M. Synthesis and Structure of a Stable Pentavalent-Uranyl Coordination Polymer. *J. Am. Chem. Soc.* **2006,** *128*, 7152-7153.

(10) Mougel, V.; Horeglad, P.; Nocton, G.; Pécaut, J.; Mazzanti, M. Cation–Cation Complexes of Pentavalent Uranyl: From Disproportionation Intermediates to Stable Clusters. *Chemistry – A European Journal* **2010,** *16*, 14365-14377.

(11) Arnold, P. L.; Patel, D.; Wilson, C.; Love, J. B. Reduction and Selective Oxo Group Silylation of the Uranyl Dication, *Nature* **2008,** *451*, 315.

(12) Schnaars, D. D.; Wu, G.; Hayton, T. W. Reduction of pentavalent uranyl to U(IV) facilitated by oxo functionalization. *J. Am. Chem. Soc.* **2009,** *131*, 17532-17533.

(13) Hayton, T. W.; Wu, G. Exploring the Effects of Reduction or Lewis Acid Coordination on the U═O Bond of the Uranyl Moiety. *Inorg. Chem.* **2009,** *48*, 3065-3072.

(14) Schnaars, D. D.; Wu, G.; Hayton, T. W. Silylation of the Uranyl Ion Using $B(C_6F_5)_3$-Activated Et_3SiH. *Inorg. Chem.* **2011**, *50*, 9642-9649.

(15) Pedrick, E.; Wu, G.; Kaltsoyannis, N.; Hayton, T. Reductive silylation of a uranyl dibenzoylmethanate complex: an example of controlled uranyl oxo ligand cleavage. *Chem. Sci.* **2014**, *5*, 3204-3213.

(16) (a) Arnold, P. L.; Puig-Urrea, L.; Wells, J. A. L.; Yuan, D.; Cruickshank, F. L.; Young, R. D. Applications of boroxide ligands in supporting small molecule activation by U(III) and U(IV) complexes. *Dalton Trans.* **2019,** *48*, 4894-4905. (b) Faizova, R.; Fadaei-Tirani, F.; Bernier-Latmani, R.; Mazzanti, M. Ligand-Supported Facile Conversion of Uranyl(VI) into Uranium(IV) in Organic and Aqueous Media. *Angew. Chem. Int. Ed.* **2020,** *59*, 6756-6759.

(17) Kumar, A.; Lionetti, D.; Day, V. W.; Blakemore, J. D. Redox-inactive metal cations modulate the reduction potential of the uranyl ion in macrocyclic complexes. *J. Am. Chem. Soc.* **2020**, *142*, 3032-3041.

(18) Mikeska, E. R.; Blakemore, J. D. Evidence for Reactivity of Decamethylcobaltocene with Dichloromethane. *Organometallics* **2023,** *42*, 1444-1447.

(19) Bell, N. L.; Shaw, B.; Arnold, P. L.; Love, J. B. Uranyl to uranium (IV) conversion through manipulation of axial and equatorial ligands. *J. Am. Chem. Soc.* **2018**, *140*, 3378-3384.

(20) Kersten, B.; Hawthorne, K.; Williamson, M.; Akolkar, R.; Duval, C. E., The Future of Nuclear Energy: Electrochemical Reprocessing of Fuel Takes Center Stage. *Electrochem. Soc. Interface* **2021,** *30*, 53-57.

(21) (a) Mougel, V.; Pécaut, J.; Mazzanti, M. New polynuclear U(IV)–U(V) complexes from U(IV) mediated uranyl(V) disproportionation. *Chem. Commun.* **2012**, *48*, 868-870. (b) Chatelain, L.; Tuna, F.; Pécaut, J.; Mazzanti, M. A zig-zag uranyl(v)–Mn(ii) single chain magnet with a high relaxation barrier. *Chem. Commun.* **2015,** *51*, 11309-11312.

(22) Takeyama, T.; Tsushima, S.; Takao, K. Effects of Substituents on the Molecular Structure and Redox Behavior of Uranyl(V/VI) Complexes with N_3O_2-Donating Schiff Base Ligands. *Inorg. Chem.* **2021,** *60*, 11435-11449.

(23) Mikeska, E.R., Benitez, G.M., Zhang, K., Oliver, A.G., Caricato, M.,* Comadoll, C.G.,* and Blakemore, J.D.,* Evidence for Ligand- and Metal-Centered Reduction in Polypyridyl Dicarboxylate Complexes of Ru(II) and U(VI), *Available on ChemRxiv*, **2022**, doi: 10.26434/chemrxiv-2022-jbc9n

(24) Cattalini, L.; Degetto, S.; Vidali, M.; Vigato, P. A., Uranyl complexes containing polydentate schiff bases. *Inorg. Chim. Acta* **1972,** *6*, 173-176.

(25) Zanello, P.; Connelly, N. G. *Inorganic Electrochemistry: Theory, Practice and Application*; Royal Society of Chemistry: Cambridge, 2003; pp 55–58.

(26) Savéant, J.-M. *Elements of Molecular and Biomolecular Electrochemistry*; Wiley: Hoboken, NJ, 2019.

(27) Connelly, N. G.; Geiger, W. E. Chemical redox agents for organometallic chemistry. *Chem. Rev.* **1996**, *96*, 877-910.

(28) Mizuoka, K.; Tsushima, S.; Hasegawa, M.; Hoshi, T.; Ikeda, Y. Electronic Spectra of Pure Uranyl(V) Complexes: Characteristic Absorption Bands Due to a $U^VO_2^+$ Core in Visible and Near-Infrared Regions. *Inorg. Chem.* **2005**, *44*, 6211–6218.

(29) Mizuoka, K.; Kim, S.-Y.; Hasegawa, M.; Hoshi, T.; Uchiyama, G.; Ikeda, Y. Electrochemical and Spectroelectrochemical Studies on UO_2 (saloph) L (saloph= N, N'-Disalicylidene-o-phenylenediaminate, L= Dimethyl Sulfoxide or N, N-Dimethylformamide). *Inorg. Chem.* **2003**, *42*, 1031−1038.

(30) Mayer, R. J.; Hampel, N.; Ofial, A. R. Lewis Acidic Boranes, Lewis Bases, and Equilibrium Constants: A Reliable Scaffold for a Quantitative Lewis Acidity/Basicity Scale. *Chem. – Eur. J.* **2021**, *27*, 4070-4080.

(31) Costentin, C.; Savéant, J.-M. Concepts and tools for mechanism and selectivity analysis in synthetic organic electroche istry. *Proc. Natl. Acad. Sci. U. S. A.* **2019**,*116*, 11147−11152.

(32) Sarsfield, M. J.; Helliwell, M. Extending the chemistry of the uranyl ion: Lewis acid coordination to a UO oxygen. *J. Am. Chem. Soc.* **2004,** *126*, 1036-1037.

(33) Cooper, O.; Camp, C.; Pecaut, J.; Kefalidis, C. E.; Maron, L.; Gambarelli, S.; Mazzanti, M. Multimetallic cooperativity in uranium-mediated CO_2 activation. *J. Am. Chem. Soc.* **2014,** *136*, 6716-6723.

(34) Kindra, D. R.; Evans, W. J. Magnetic susceptibility of uranium complexes. *Chem. Rev.* **2014,** *114*, 8865-8882.

(35) Reactivity experiments using ^{1}H NMR and UV-visible spectroscopy indicate that Cp^*_2Co can slowly reduce BPh_3 (Figures S12, S13, and S55-S57). We elected to add borane after reduction of uranium in our synthetic work to disfavor this minor albeit accessible cross-reaction pathway.

(36) In accord with the possibility of $\mathbf{U^{IV}B_2}$ decomposition, multiple attempts to grow crystals of this species did not result in crystals of the compound suitable for X-ray diffraction analysis. Instead, on two occasions, crystals were obtained and diffracted that correspond to $[Ph_3BO]^-[Cp^*_2Co]^+$. The structure of this species is described in the Supporting Information (pp. S95 and S96), and is consistent with cleavage of a U–O_{oxo} bond upon reduction and borylation of $\mathbf{U^{VI}}$. The conditions under which these crystals were obtained correspond to those required for generation of stoichiometric quantities of $\mathbf{U^{IV}B_2}$ and $\mathbf{U^{V}B_1}$. Our working model for the solution reactivity of $\mathbf{U^{V}B_1}$ implicates generation of $\mathbf{U^{IV}B_2}$, a species that could decompose to form $[Ph_3BO]^-[Cp^*_2Co]^+$.

(37) Graves, C. R.; Scott, B. L.; Morris, D. E.; Kiplinger, J. L. Facile access to pentavalent uranium organometallics: one-electron oxidation of uranium (IV) imido complexes with copper (I) salts. *J. Am. Chem. Soc.* **2007,** *129*, 11914-11915.

(38) Arnold, P. L.; Hollis, E.; Nichol, G. S.; Love, J. B.; Griveau, J.-C.; Caciuffo, R.; Magnani, N.; Maron, L.; Castro, L.; Yahia, A.; Odoh, S. O.; Schreckenbach, G. Oxo-Functionalization and Reduction of the Uranyl Ion through Lanthanide-Element Bond Homolysis: Synthetic, Structural, and Bonding Analysis of a Series of Singly Reduced Uranyl–Rare Earth $5f^1$-$4f^n$ Complexes. *J. Am. Chem. Soc.* **2013**, *135*, 3841-3854.

(39) Zhang, J.; Glezakou, V.-A.; Rousseau, R.; Nguyen, M.-T. NWPEsSe: An Adaptive-Learning Global Optimization Algorithm for Nanosized Cluster Systems. *J. Chem. Theory and Comput.* **2020,** *16*, 3947-3958.

(40) Becke, A. D. Density-functional thermochemistry. III. The role of exact exchange. *The Journal of Chemical Physics* **1993,** *98*, 5648-5652.

(41) Burke, K.; Perdew, J. P.; Wang, Y. Derivation of a Generalized Gradient Approximation: The PW91 Density Functional. In *Electronic Density Functional Theory: Recent Progress and New Directions*, Dobson, J. F.; Vignale, G.; Das, M. P., Eds. Springer US: Boston, MA, 1998; pp 81-111.

(42) Pantazis, D. A.; Neese, F. All-Electron Scalar Relativistic Basis Sets for the Actinides. *J. Chem. Theory Comput.* **2011,** *7*, 677-684.

(43) Weigend, F.; Ahlrichs, R. Balanced basis sets of split valence, triple zeta valence and quadruple zeta valence quality for H to Rn: Design and assessment of accuracy. *Phys. Chem. Chem. Phys.* **2005,** *7*, 3297-3305.

(44) (a) Vlaisavljevich, B.; Miró, P.; Cramer, C. J.; Gagliardi, L.; Infante, I.; Liddle, S. T. On the Nature of Actinide– and Lanthanide–Metal Bonds in Heterobimetallic Compounds. *Chem. – Eur. J.* **2011,** *17*, 8424-8433. (b) Wang, J.; Zhang, N.-X.; Wang, C.-Z.; Wu, Q.-Y.; Lan, J.-H.; Chai, Z.-F.; Nie, C.-M.; Shi, W.-Q. Theoretical probing of twenty-coordinate actinide-centered boron molecular drums. *Phys. Chem. Chem. Phys.* **2021,** *23*, 26967-26973. (c) Zhao, R.-N.; Yuan, Y.; Han, J.-G.; Duan, Y. Actinide elements and germanium: a first-principles density functional theory investigation of the electronic and magnetic properties of ApGe (Ap = Ac–Lr) diatoms. *RSC Advances* **2014,** *4*, 59331-59337. (d) Niu, K.; Yang, F.; Gaudin, T.; Ma, H.; Fang, W. Theoretical Study of Effects of Solvents, Ligands, and Anions on Separation of Trivalent Lanthanides and Actinides. *Inorg. Chem.* **2021,** *60*, 9552-9562.

(45) Löwdin, P.-O. Quantum theory of many-particle systems. I. Physical interpretations by means of density matrices, natural spin-orbitals, and convergence problems in the method of configurational interaction. *Phys. Rev.* **1955,** *97*, 1474.

(46) Davidson, E. R. *Reduced Density Matrices in Quantum Chemistry*; Academic Press: New York, 1976.

(47) Weinhold, F.; Landis, C. *Valency and Bonding, A Natural Bond Orbital Donor-Acceptor Perspective*; Cambridge University Press: Cambridge, 2005.

(48) Weinhold, F.; Landis, C.; Glendening, E. What is NBO analysis and how is it useful? *Int. Rev. Phys. Chem.* **2016,** *35*, 399-440.

(49) Weinhold, F.; Landis, C. R. Natural bond orbitals and extensions of localized bonding concepts. *Chem. Educ. Res. Pract.* **2001,** *2*, 91-104.

(50) Curtiss, L. A.; Pochatko, D. J.; Reed, A. E.; Weinhold, F. Investigation of the differences in stability of the OC···HF and CO···HF complexes. *J. Chem. Phys.* **1985,** *82*, 2679-2687.

(51) Denning, R. G. Electronic Structure and Bonding in Actinyl Ions and their Analogs. *J. Phys. Chem. A* **2007,** *111*, 4125-4143.

(52) Mirza, M.; Abdulaziz, R.; Maskell, W. C.; Wilcock, S.; Jones, A. H.; Woodall, S.; Jackson, A.; Shearing, P. R.; Brett, D. J. L., Electrochemical processing in molten salts – a nuclear perspective. *Energy Environ. Sci.* **2023,** *16*, 952-982.

(53) Li, B.; Jones, Z. R.; Eiroa-Lledo, C.; Knope, K. E.; Mocko, V.; Stein, B. W.; Wacker, J. N.; Kozimor, S. A.; Batista, E. R.; Yang, P., Structure and Dynamics of NaCl/KCl/$CaCl_2$–$EuCl_n$ (n = 2, 3) Molten Salts. *Inorg. Chem.* **2023,** *62*, 10528-10538.

TOC Graphic

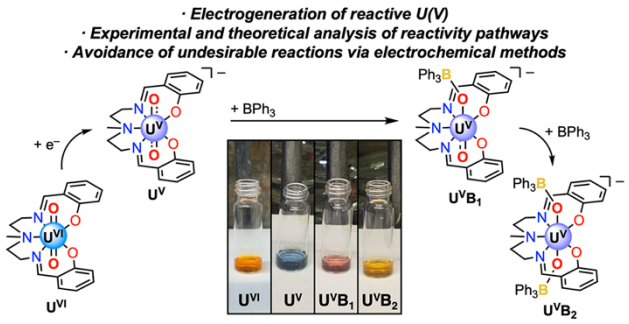

TOC Synopsis: An electrochemical approach to activation and oxo functionalization of the uranyl ion, UO_2^{2+}, is described. Clean generation of a model U(V) complex has been achieved at the surface of a carbon working electrode, and addition of a BPh_3 as electrophile results in generation of borylated species that have been fully characterized, revealing how the electrochemical reduction drives oxo functionalization. Computational work has been used to quantify the energetics and understand the electronic structures of both the isolable species and transient intermediates involved in this reactivity, affording insights into the bonding patterns that drive the electrochemical reactivity.